Available online at www.sciencedirect.com
ScienceDirect
Journal of Solid State Chemistry 180 (2007) 2896–2904
JOURNAL OF SOLID STATE CHEMISTRY
www.elsevier.com/locate/jssc

One-dimensional α-MnO_2: Trapping chemistry of tunnel structures, structural stability, and magnetic transitions

Liping Li, Yinzhen Pan, Lijuan Chen, Guangshe Li*

State Key Laboratory of Structural Chemistry, Fujian Institute of Research on the Structure of Matter, Chinese Academy of Sciences, Fuzhou 350002, PR China

Received 9 April 2007; received in revised form 15 August 2007; accepted 15 August 2007
Available online 31 August 2007

Abstract

Highly crystalline one-dimensional (1D) α-MnO_2 nanostructures were synthesized by a hydrothermal method. All samples were characterized by X-ray diffraction, transmission electron microscope, thermogravimetric and differential scanning calorimeter, and infrared spectroscopy. During the formation reactions, the tunnel structure of 1D α-MnO_2 was simultaneously modified by NH_4^+ species and water molecules. The amount of NH_4^+ species that were trapped in the tunnels is almost independent on the reaction temperature, while the total water content increased with the reaction temperature. The average diameter of α-MnO_2 nanorods increased from 9.2 to 16.5 nm when the reaction temperature increased from 140 to 220 °C. 1D α-MnO_2 was destabilized by a subsequent high-temperature treatment in air, which is accompanied by a structural transformation to 1D Mn_2O_3 of a cubic structure. At low temperatures, all 1D α-MnO_2 nanorods showed two magnetic transitions that were characterized by a decreased Néel temperature with rod diameter reduction. According to the effective magnetic moments experimentally measured, Mn ions presented in the nanorods were determined to be in a mixed valency of high spin state Mn^{4+}/Mn^{3+}.

Keywords: Nanorods; α-MnO_2; Structure stability; Magnetic transitions; Synthesis

1. Introduction

Manganese oxides are among the well-known natural and synthetic materials that have shown outstanding structural flexibility and physical and chemical properties for potential applications as ionic or molecular sieves, catalysts, cathode materials of secondary rechargeable batteries, and electro-chromic and new magnetic materials [1]. Most of these applications are beneficial to the plenty of polymorphs including α-, β-, γ-, and δ-MnO_2 phases that manganese dioxides have [2]. Structure–property relationships of the manganese oxides as 1D nanostructures can provide information on model material design of novel properties for many aspects of technological uses. Several methods have been reported in literature to prepare various phases of 1D MnO_2, and significant advances have been achieved especially in the case of α-MnO_2 compounds [3]. However, the literature results about 1D α-MnO_2 nanostructures are very difficult to compare and seem inconsistent. An explanation could be the lack of the knowledge about the trapping chemistry of inorganic species in the tunnels of α-MnO_2 nanostructures.

α-MnO_2 exhibits a special tunnel structure, in which MnO_6 octahedra share their corners with each other parallel to the *a–b* plane to form 2×2 tunnels [4]. The effective diameters of tunnel are about 0.26 nm for a bottleneck on (0 0 2) plane and about 0.48 nm on (0 0 1) plane [5]. These tunnel features also render α-MnO_2 with excellent adsorption properties [6], while these tunnels are alternatively easily contaminated by adsorbing certain inorganic species from the reaction systems. Consequently, the chemical compositions of 1D α-MnO_2 nanostructures can vary in uncontrolled ways, imposing huge uncertainties in determining and/or understanding many aspects of structural and physical properties. Moreover, most, if not all, of the formation reaction mechanisms proposed in literatures [3a,3b,7], for 1D α-MnO_2 had excluded the influences of

*Corresponding author.
E-mail address: guangshe@fjirsm.ac.cn (G. Li).

0022-4596/$ - see front matter © 2007 Elsevier Inc. All rights reserved.
doi:10.1016/j.jssc.2007.08.017

the trapped species on the chemical compositions and stability of the tunnel structures. As a result, the phase evolutions of this tunnel structure of α-MnO_2 still remains in debate. For instance, some larger cations, such as K^+, could be trapped in the tunnels by stabilizing the special tunnel structure [8]. While in many cases, insertion of large cationic ions into MnO_2 can also destabilize the tunnel structures by forming layered structures [9], mixed phases, or low crystallinity compounds [10], depending on the ionic sizes of the trapped cations. Recently, Kijima et al. [5] and Feng et al. [11] concluded that α-MnO_2 can be stabilized without larger stabilizing cations. Water molecules show a strong affinity for α-MnO_2 and therefore can be readily trapped in the tunnels. These trapped chemical species cannot be removed by ion exchange, since an increase in water content can give rise to the occurrence of Mn^{3+} and the resulting larger lattice dimensions [11–13]. Consequently, the structural difference originated from the chemical compositions can have significant impacts on the material morphology due to the specific growth of individual particles in respect with the lattice structure and dimensions. In comparison with other trapped ions, insertion of NH_4^+ in the tunnels is advantageous in providing information on the comprehension of trapping chemistry and structural stability of the tunnel structure of α-MnO_2 for many technological uses (e.g., in stabilizing the lithium batteries during the lithium insertion/extraction) [14], because (1) NH_4^+ species has a relatively small ionic size of 0.143 nm for tunnel decoration, (2) NH_4^+ ions have favorable hydrogen bonding ability and Lewis base characteristics for partial filling of the lattice vacancies available within the 2×2 tunnels, and (3) NH_4^+ species can be easily removed at relatively low temperatures for retaining the 1D morphologies for low-dimensional property and application studies.

It is therefore of technological interest to elucidate the quantitative determination of the trapping chemistry of NH_4^+ species and water molecules in the tunnels and its relevance to the structural stabilities of 1D α-MnO_2. In this work, we hydrothermally prepared single-phase and highly crystalline 1D α-MnO_2 with tunnels being modified by NH_4^+ and water molecules by taking good reference of the successful synthesis of various morphologies including helical fibers [15], nanowires [16], nanorod [3], and nanoneedle of α-MnO_2 [5]. We also quantitatively determined the contents of NH_4^+ ions and water molecules and further explored the physical dimension dependence of thermal stability and magnetic transitions. We clearly demonstrated that the Mn ions were in a mixed valency of Mn^{4+}/Mn^{3+} in our samples. It is surprising that Mn^{3+} ions are revealed to be in a high-spin state, which is contrast to the low-spin Mn^{3+} reported in literature for potassium counterparts.

2. Experimental section

Analytical grade chemicals, $(NH_4)_2S_2O_8$, $MnSO_4\cdot H_2O$, and $(NH_4)_2SO_4$ were used as the starting materials. Firstly, given amounts of starting materials were weighted according to the molar ratios of $(NH_4)_2S_2O_8$:$MnSO_4\cdot H_2O$:$(NH_4)_2SO_4 = 1{:}1{:}x$ in the range of $x = 0$–5, which were then dissolved into 30 ml water to get a clear solution. This solution was transferred to a 32 ml Teflon lined autoclave which was put into an oven to react at 120 °C for 12 h. After cooling to room temperature naturally, the resulting black solid product was filtered and washed thoroughly with distilled water, and dried at 120 °C for 4 h. The samples thus obtained were named as M120(x), where x(= 0, 1.8, 3.75, and 5) denotes the molar ratio of $(NH_4)_2SO_4$ to $MnSO_4\cdot H_2O$. The second experiment employed a fixed molar ratio of $(NH_4)_2S_2O_8$:$MnSO_4\cdot H_2O$:$(NH_4)_2SO_4$ at 1:1:5 in which the reaction temperature was increased to 140, 180, and 220 °C, respectively. The samples were named by similar denotation as M140(5), M180(5), and M220(5), respectively.

The structures and phase compositions of the samples were characterized by X-ray diffraction (XRD) on Rigaku DMAX2500 X-ray diffractometer using a copper target. The average grain sizes, D, of α-MnO_2 phase were measured from the most intense XRD peak (3 1 0) using Scherrer formula, $D = 0.9\lambda/\beta\cos\theta$, where λ is the X-ray wavelength employed, θ is the diffraction angle of the most intense peak (3 1 0), and β is defined as the half width after subtracting the instrumental broadening. The morphologies of the samples were determined using transmission electron microscopy (TEM) on a JEM-2010 apparatus with an acceleration voltage of 200 kV.

Nitrogen concentration of the samples was determined by a combustion method using Varia EL III elemental analyzer. The valence states of Mn ions in the samples were analyzed by a titration method [17]. Total electron number involved in oxidation–reduction was determined by the standard potassium permanganate–oxalic acid redox back titration. The amount of manganese in the sample was determined by ethylene diamine tetraacetic acid (EDTA) complexometric titration. Several additional titration experiments were carried out for each sample and the average value was finally taken as the valence state of Mn ions. Specific surface areas of the samples were measured by N_2 adsorption isotherms at 77 K in a relative pressure range $P/P_0 = 0.05-0.3$ (P_0 = saturation pressure and P = equilibrium pressure) using a Micromeritics ASAP 2000 Surface Area and Porosity Analyzer.

Infrared spectra of the samples were recorded on Perkin-Elmer IR spectrophotometer using a KBr pellet technique. The thermal behaviors of the samples were examined using simultaneous differential scanning calorimetry (DSC) and thermogravimetric analysis (TGA). The measurements were performed at a heating rate of 15 °C/min from room temperature to 1200 °C in air. Zero-field-cooled (ZFC) magnetization curves of the samples were recorded from 2 K to room temperature under an applied magnetic field H of 10 kOe using a Quantum Design PPMS-7 magnetometer. All data were obtained by first cooling the samples from room temperature in zero applied field to 2 K. Then, a

field was applied and the variation of magnetization was measured with increasing temperature up to room temperature.

3. Results and discussion

3.1. Synthesis of highly crystalline 1D α-MnO_2

The phase content of α-MnO_2 is usually controlled by two factors: NH_4^+ concentration and reaction temperature. The influence of NH_4^+ concentration on the formation reaction of α-MnO_2 phase was investigated by varying the initial molar ratios of starting materials, while the reaction temperature was fixed at 120 °C. Fig. 1 shows XRD patterns of the products obtained at given initial molar ratios of $(NH_4)_2S_2O_8$:$MnSO_4 \cdot H_2O$:$(NH_4)_2SO_4$ = 1:1:x. The standard diffraction data for α-MnO_2 (JCPDS No. 44-0141) and γ-MnO_2 (ICSD-78331) were also shown for comparison. At $x = 0$, several intensive diffraction peaks appeared at $2\theta = 12.4°$, 17.8°, 37.4°, and 49.6°, which are ascribed to α-MnO_2. The additional diffraction peaks were also observed at $2\theta = 22.25°$, 35.18°, and 38.5° which are all characteristic of γ-MnO_2. Therefore, when no $(NH_4)_2SO_4$ was involved in the reaction systems, the products were a mixture of α- and γ-MnO_2. With increasing x, the characteristic diffraction peak for γ-MnO_2 at $2\theta = 22.25°$ became weaker in intensity, indicating the decrease in the amounts of γ-MnO_2. However, when the initial molar ratio was increased to $x = 5$, the sample obtained was still a mixed phase of α- and γ-MnO_2 as indicated by the occurrence of a weak diffraction peak at $2\theta = 22.25°$. These results indicated that the concentration of NH_4^+ plays a key role in the formation of α-MnO_2.

Influence of reaction temperatures on the formation of α-MnO_2 phase was investigated by increasing the preparation temperatures from 140 to 220 °C, while the initial ratio was fixed at $x = 5$. Fig. 2 shows the XRD patterns of the

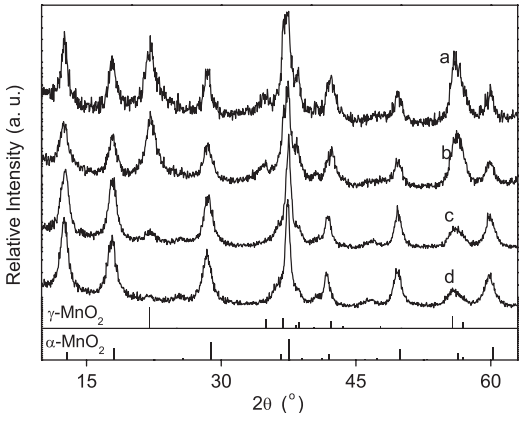

Fig. 1. XRD patterns of the products prepared at 120 °C with varied molar ratios of $(NH_4)_2S_2O_8$:$MnSO_4 \cdot H_2O$:$(NH_4)_2SO_4$ = 1:1:x at (a) $x = 0$, (b) $x = 1.8$, (c) $x = 3.75$, and (d) $x = 5$. Vertical bars at the bottom represent the standard diffraction data for γ- and α-MnO_2 from ICSD-78331 and JCPDS (No. 44-0141).

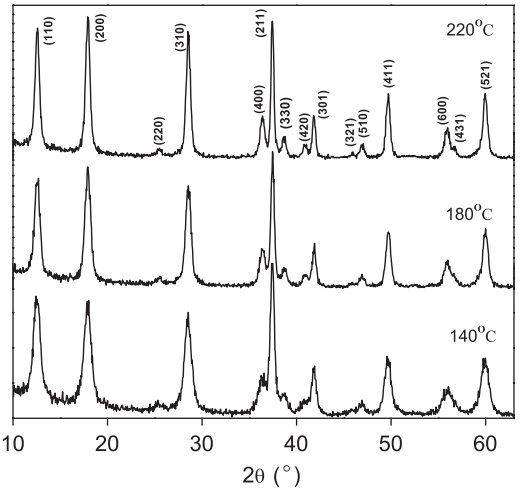

Fig. 2. XRD patterns of the samples prepared at given hydrothermal temperatures when the molar ratio of $(NH_4)_2S_2O_8$:$MnSO_4 \cdot H_2O$:$(NH_4)_2SO_4$ is fixed at 1:1:5.

products prepared at given temperatures. It is seen that all diffraction peaks matched well the standard diffraction data of α-MnO_2, while no traces of γ-MnO_2 were detected. Therefore, high reaction temperatures favor to the formation of single-phase α-MnO_2. With increasing the reaction temperature, all diffraction peaks became narrowed, which is associated with an increase in the physical dimension of α-MnO_2 nanostructure. The particle size of the sample obtained at 140 °C calculated from the peak (310) using Scherrer formula was only 9.2 nm, which was increased to 16.5 nm after hydrothermal reaction at 220 °C for 12 h (Table 1). Comparatively, peak (211) at $2\theta = 37.5°$ is very sharp for all samples. The particle dimensions estimated from this peak width were about 18 and 26 nm for M140(5) and M220(5), respectively. The presence of sharp peak (211) implies that α-MnO_2 particles are highly oriented which is confirmed by our TEM observations as described latter.

Morphologies of the samples were examined by TEM observations. All α-MnO_2 samples showed a uniform nanorod shape. For the samples prepared at lower hydrothermal temperatures, such as M120(5), all rods are very tiny (Fig. 3(a)). When the hydrothermal temperature was increased, the rod diameter became larger. For example, sample M220(5) showed a rod diameter of about 18 nm on average and the length ranging from 0.2 to 1 μm (Fig. 3(b)). The diameters of these nanorods observed by TEM were very close to the particle sizes calculated using Scherrer formula for diffraction peak (310). These nanorods were also examined by HRTEM. As shown in Fig. 3(c), sample M220(5) is a structurally uniform assembly of single crystals. The interlayer spacing was 0.310 nm, which is consistent with the corresponding (310) plane. Careful analysis for all HRTEM images indicated that all nanorods grew along c-axis, the direction of the tunnels. Diffraction peaks (2 1 1) of all samples have the "c" component and therefore showed a relatively narrow peak width in

Table 1
Physical parameters of 1D α-MnO_2 nanostructures

Samples	Diameter (nm)	Lattice dimensions		$(\Delta m/m)_{total}$[a] (%)	Chemical formula: $(NH_4)_xMnO_{2-\delta}\cdot yH_2O$	Magnetic parameters[b]	
		a (nm)	*c* (nm)			*C* (emu K/mol Oe)	θ (K)
M140(5)	9.2	0.9874(2)	0.28558(3)	18.5	$x=0.12$, $y=0.25$, $\delta=0.002$	1.94	−308
M180(5)	11.9	0.9866(1)	0.28561(2)	17.7	$x=0.12$, $y=0.19$, $\delta=0.015$	1.97	−337
M220(5)	16.5	0.9856(1)	0.28540(3)	22.2	$x=0.14$, $y=0.46$, $\delta=0.020$	2.04	−336

[a]$(\Delta m/m)_{total}$ represents the relative mass variations at temperature up to 1200 °C.
[b]Magnetic data are obtained by fitting the experimental data using Curie–Weiss law. *C* and θ denote the Curie–Weiss constant and temperature, respectively.

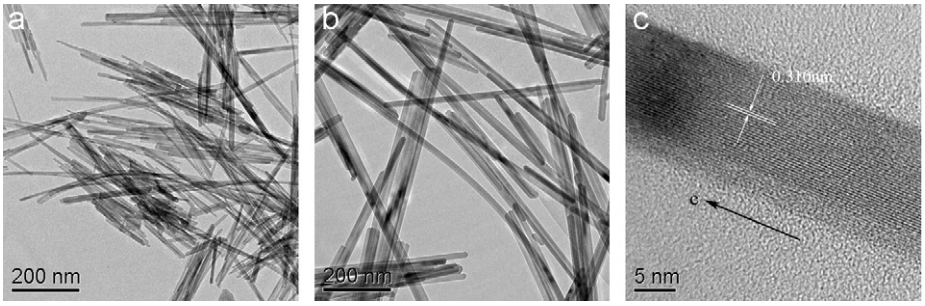

Fig. 3. TEM images of 1D α-MnO_2 (a) M120(5) and (b) M220(5), and (c) HRTEM image of individual rod of M220(5).

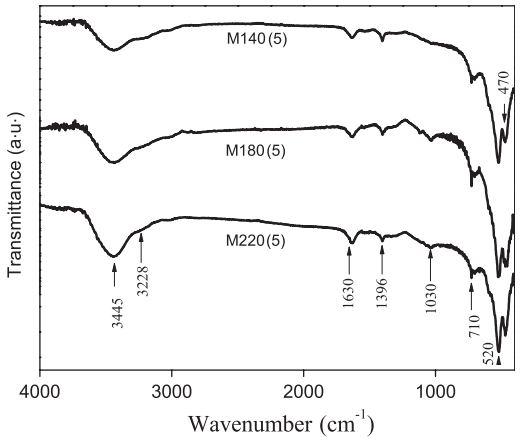

Fig. 4. Infrared spectra of samples M140(5), M180(5), and M220(5).

comparison with other diffraction peaks without "*c*" component.

The chemical compositions of the as-prepared 1D α-MnO_2 nanostructures were investigated by IR spectra in combination with chemical analysis and valence determination by titration methods. Fig. 4 shows the IR spectra of the samples. The absorption peaks for all samples showed much closer positions. Two broad absorptions observed at 3445 and 3228 cm^{-1} for these 1D MnO_2 nanostructures were assigned to the stretching vibrations of –OH group of adsorbed water, while that at 1630 cm^{-1} is due to the bending vibration of –OH group. The sharp vibrations at about 470, 520, and 710 cm^{-1} were contributed by the vibrations of Mn–O bonds as reported for many manganese oxides [18,19a]. According to the literature, the weak band observed at 1030 cm^{-1} is associated with the vibration of Mn^{3+}–O bond [19a], which indicates the presence of traces of Mn^{3+} in these nanorods. The absorption peak centered at about 1396 cm^{-1} was characteristic of NH_4^+ species [19b]. These results are consistent with the previous literature work, in which NH_4^+ ions are trapped in the tunnel of α-MnO_2 structure [4]. From Fig. 4, it can be found that the relative intensity of stretching vibrations of –OH as well as of the vibration of Mn^{3+}–O bond became more pronounced with preparation temperature (or the rod diameter). Elemental analyses of these nanorods indicated that the mass percentage of nitrogen was 2.04%, 1.75%, and 1.75% for samples M220(5), M180(5), and M140(5), respectively. The existence of nitrogen (also NH_4^+ species) in the tunnels of 1D MnO_2 nanostructures was also confirmed by the TG–MS measurement (not shown). The corresponding average valences of Mn ions in these samples were 3.88($\pm$0.01), 3.92($\pm$0.01), and 3.90($\pm$0.01) as determined by a titration method. These results clearly demonstrated a

mixed valence of Mn ions in the nanorods, just like what is observed in many manganese oxides [13]. Therefore, the formula for as-prepared 1D α-MnO_2 nanostructures can be described as $(NH_4)_xMnO_{2-\delta}\cdot yH_2O$, where x and y denote the molar ratio of NH_4^+ species and water molecules absorbed in the tunnels and/or on surfaces, and δ represents the number of oxygen vacancies originated from the presence of mixed valence of Mn ions.

As stated above, α-MnO_2 has a special 2×2 channel structure which can trap other inorganic species from the reaction systems. Therefore, formation mechanism of 1D α-MnO_2 could be understood in terms of the preparation parameter of ammonia concentration and temperature as well as the relative phase stability of manganese dioxides. Concerning the role of reaction temperature, our preliminary preparation demonstrated that α-MnO_2 is stable in the presence of $(NH_4)_2SO_4$ when the reaction temperature is above 140 °C. While with regards to the ammonia, we have indicated that γ-MnO_2 is stable at the absence of ammonia species or at low temperatures (Fig. 1), which can partly transform into α-MnO_2 in the presence of 5% ammonia solution [20]. Thus, ammonia concentration and reaction temperature are two dominant preparation factors in forming single-phase α-MnO_2, probably via the following reaction route:

$$MnSO_4 + (NH_4)_2S_2O_8 + 2H_2O \rightarrow \gamma\text{-}MnO_2 + (NH_4)_2SO_4 + 2H_2SO_4 \quad (1)$$

$$\gamma\text{-}MnO_2 + xNH_4^+ + (x+y)H_2O \rightarrow (NH_4)_xMnO_{2-\delta}\cdot yH_2O\,(\alpha\text{-phase}) + 2xH^+ + \frac{x+\delta}{2}O_2 \quad (2)$$

If ammonia concentration was high enough, γ-MnO_2 would react with NH_4^+ and transform into α-MnO_2 with the tunnels being decorated with ammonia species and water molecules. Therefore, increasing the ammonia concentration could promote the reaction in Eq. (2) for a complete formation of 1D α-MnO_2. This assumption is confirmed by our XRD analysis (Fig. 1). From reaction Eq. (2), it is also noted that oxygen partial pressure could affect the content of trapping ions in the tunnel of α-MnO_2. In present hydrothermal reaction systems, $(NH_4)_2S_2O_8$ could act as an effective oxidant. When some NH_4^+ ions are trapped in the tunnel, Mn^{2+} ions would not be completely oxidized to Mn^{4+}. Increase of oxygen partial pressure in reaction system would be beneficial for the oxidization of Mn^{2+} to Mn^{4+}, which possibly reduces the amount of NH_4^+. Single-phase α-MnO_2 can also be formed by reducing the concentration of $(NH_4)_2S_2O_8$ [3b]. Increasing reaction temperature resulted in an increase in $(NH_4)_xMnO_{2-\delta}$ (α-phase) content. The formation of single-phase α-MnO_2 at temperatures higher than 140 °C is thus closely related to the decrease of Gibbs free energies. The transformation from γ- to α-MnO_2 revealed by Eq. (2) can be understood by the polymorphic transformation induced by point defect, since γ-MnO_2 comprises a complex microstructure that includes (i) de Wolff disorder (intergrowths of pyrolusite and ramsdellite) [21], (ii) microtwinning about the (0 2 1) and (0 6 1) planes of ramsdellite [22], and (iii) point defects such as Mn^{4+} vacancies and Mn^{3+} substitutions [23]. Pyrolusite structure is isostructural with rutile TiO_2 which comprises 1×1 octahedra. Simulation reveals that pyrolusite structure formed by re-crystallization of all the surrounding amorphous MnO_2 is heavily twinned and comprises a wealth of isolated and clustered point defects [24]. The existence of point defects and ramsdellite structure (1×2 octahedral) would lead to the transformation of γ- to α-MnO_2 under suitable reaction conditions such as given concentration of NH_4^+ and high temperatures.

3.2. Structural stability of 1D α-MnO_2 nanostructures at high temperatures

Thermal stability and phase evolution of 1D α-MnO_2 were studied by TGA–DTA measurements in combination with XRD analysis. Fig. 5 shows the TGA data of the samples. It is clear that all 1D MnO_2 showed similar TGA curves except for the amounts of mass losses. In DTA curve of sample M220(5), three distinct endothermic peaks were observed at about 135, 535, and 930 °C, which corresponded to three mass losses in TGA curves. The first mass loss that occurred in a broad temperature range from 70 to 460 °C is ascribed to the loss of absorbed water on surfaces or in the tunnel cavity. With regards to the two sharp mass losses at higher temperatures, we monitored the phase evolution of 1D MnO_2 by measuring the XRD patterns of the samples quenched in the TG cell from 650 or 1200 °C in air. As illustrated in Fig. 6, the product quenched from 650 °C crystallized in a pure cubic α-Mn_2O_3, while that quenched from 1200 °C was Mn_3O_4. To confirm existence of the water and ammonium molecules trapped in the tunnels, α-MnO_2 sample was heated from 35 to 1100 in N_2 atmosphere at a flux of 20 ml/min, and the exhaust gases released were examined by mass spectroscopy. It was found that water and ammonia in the tunnel were released from 200 to 400 °C

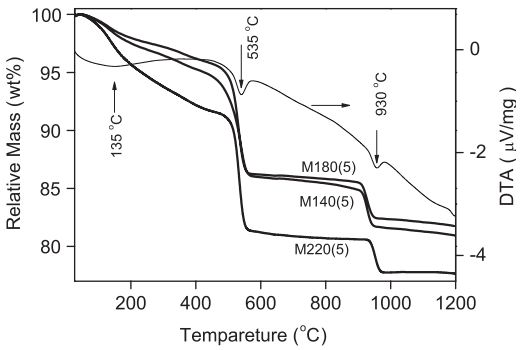

Fig. 5. TGA data of samples M140(5), M180(5), and M220(5), and DTA curve of M220(5).

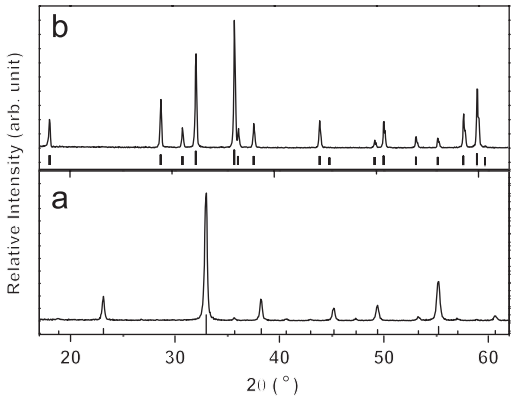

Fig. 6. XRD patterns of the products quenched from (a) 650 °C and (b) 1200 °C. Standard diffraction data of Mn_2O_3 and Mn_4O_3 are shown as vertical bars at the bottom of (a) and (b), respectively.

(not shown). These results indicated that 1D α-MnO_2 nanostructures were not stable at high temperatures and might show a phase evolution according to the following routes:

$$(NH_4)_xMnO_{2-\delta}\cdot yH_2O \rightarrow \frac{1}{2}Mn_2O_3 + xNH_3 + \left(\frac{x}{2}+y\right)H_2O + \frac{(1-2\delta-x)}{4}O_2, \quad 200<T<580\,^{\circ}C \tag{3}$$

$$3Mn_2O_3 \rightarrow 2Mn_3O_4 + \frac{1}{2}O_2, \quad T>930\,^{\circ}C \tag{4}$$

Basing on the elemental analysis results, valence states of Mn ions, and relative mass variations ($\Delta m/m_{total}$) at temperatures up to 1200 °C, chemical compositions of as-prepared α-MnO_2 nanorods were determined and given in Table 1. The content of NH_4^+ ions for all samples was almost the same within the experimental errors and smaller than the theoretical ratio of tunnel/Mn = 0.25 [12]. This indicated that hydrothermal temperature (also rod diameter) has little influence on the trapping of NH_4^+ ions in the tunnels of α-MnO_2. On the other hand, it is noted that absorbed water existed in all samples, among of which sample M220(5) gave the largest amounts of water content which is in contrary to the trend of particle dimension dependence of water content for many other nanoscale oxides. For the latter cases, the water content usually decreased with increasing particle dimension [25].

Water molecules might be trapped in the tunnels of α-MnO_2. For the present 1D α-MnO_2, the content of absorbed water should come from two primary contributions: surface hydration molecules (including physical and chemical absorbed ones) and trapped molecules in the tunnels. The binding energy of chemisorbed water molecules to the tunnel surfaces is usually high, which results in a significant increase in dehydration temperature up to 300 °C or more [25,26]. It is impossible to distinguish these two types of water molecules by TG–DTA in particular for the present tunneled nanostructures. Nevertheless, we got useful information by comparing to the water contents absorbed on the condensed nanostructures. It is noted that the content of absorbed water on the surface of nanoparticles is dependent on the surface area. A large surface area is expected to give plenty of water molecules absorbed. BET measurement showed that the surface areas were 100, 84, and 64 m^2/g for samples M140(5), M180(5), and M220(5), respectively. For the materials with tunnel structure, surface areas should come from two contributions: inner and outside surface. At a first approximation, the inner surface contribution is assumed to be constant for all nanorods because of the same crystal structure. This means that the water content from surface hydration should decrease with increasing diameter of α-MnO_2 nanorods, which is opposite to what we observed in this work. So, it is reasonable that some amounts of water molecules were likely trapped in the tunnels of 1D α-MnO_2 with their content increasing with preparation temperature and/or the rod diameter.

The morphological evolution of 1D MnO_2 was examined by TEM and HRTEM observations. Fig. 7 shows the TEM and HRTEM images of the product Mn_2O_3 obtained after quenching M220(5) from 650 °C. Similar to the as-prepared α-MnO_2 nanorods, the quenched product of Mn_2O_3 still maintained the rod shape. From TEM images in Figs. 3(a) and 7(a), it can be seen that the 1D rods of the quenched product are slightly different from as-prepare nanorods. The quenched product presented an uneven rod-like shape,

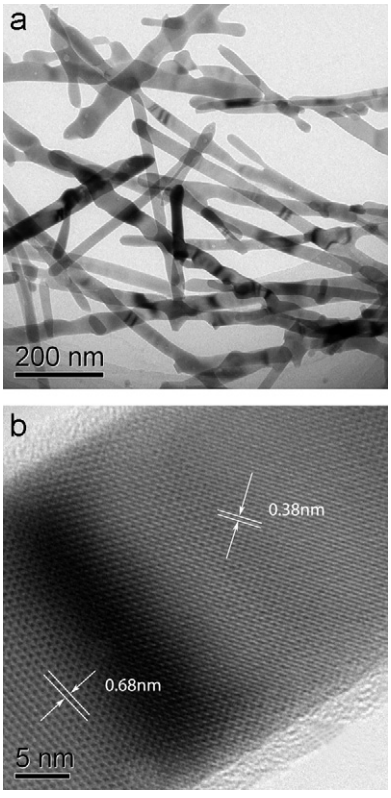

Fig. 7. TEM (a) and HRTEM (b) images of the products of cubic Mn_2O_3 quenched from 650 °C.

which compares to the uniform distribution of nanorods in as-prepared α-MnO_2. The uneven nanorods of the quenched samples are mainly associated with the contact of rods at high temperatures since rods getting in touch with each other could result in a significant inner growth, for example, the rods exhibited a wide distribution of diameters from 16 to 60 nm. This uneven characteristic also resulted in the occurrence of defects, as revealed by HRTEM. As shown in Fig. 7(b), different lattice planes were observed in these rods. The lattice fringes with $d = 0.38$ nm corresponded to (2 1 1) plane, while those with $d = 0.68$ nm to (1 1 0) plane. These lattice planes are assigned to the cubic phase of Mn_2O_3, which is different from the orthorhombic Mn_2O_3 nanorods when precursor γ-MnOOH was heated at high temperatures [27]. The retaining 1D morphology from α-MnO_2 to cubic Mn_2O_3 can be understood in terms of the tunnel structural characteristics and trapping chemistry of NH_4^+ and water. For most nanostructures, the lattice symmetry of the precursors directly determines the morphology and phases of the final products [28]. α-MnO_2 belongs to a tetragonal structure, in which double chains of edge-sharing octahedral extend in two direction and share corners to form tunnels. The bonds between NH_4^+ and oxygen ions in the tunnels would be broken at high temperatures. Two NH_4^+ ions at the neighborhood combined with one oxygen and release one H_2O and two NH_3 molecules. The oxygen species left would move along *c*-axis to form a structure with sharing corner of MnO_6 octahedra. For tetragonal structure of α-MnO_2, the variations of *a*- and *b*-axis should be the same. Therefore, the decomposition product of α-MnO_2 is cubic Mn_2O_3, which compares to the orthorhombic Mn_2O_3 prepared by firing monoclinic γ-MnOOH [27].

3.3. Magnetic transitions of 1D α-MnO_2

Finite size effects on lattice dimensions of 1D α-MnO_2 nanostructures were determined by structural refinements. The lattice parameters of all samples were listed in Table 1, which are very close to the values reported previously [4,5]. With increasing the rod diameter, the lattice parameters showed no apparent changes within the experimental errors.

Finite size effects on the magnetic transition temperatures of α-MnO_2 nanorods were investigated by measuring the temperature dependences of magnetization of the samples under the zero field cooling and at an applied field of 10 kG. Fig. 8(a) shows the temperature dependence of mass susceptibility. During the heating process, an obvious hump was first observed in a narrow temperature range from 9 to 14 K for M140(5) and M220(5). Then all samples went through another magnetic transition, as indicated by the kinks observed in the temperature range from 20 to 25 K. Further increasing temperature from 30 K to room temperature, the magnetization of all α-MnO_2 nanorods decreased, indicating a paramagnetic behavior.

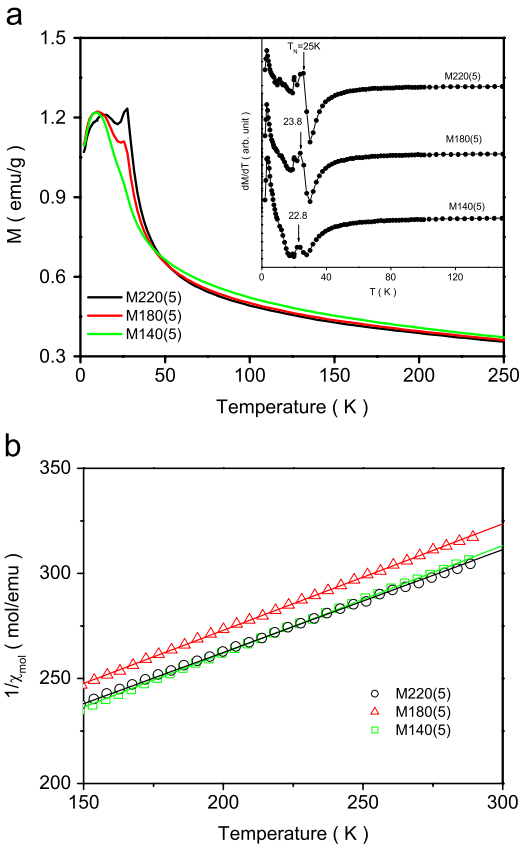

Fig. 8. (a) Temperature dependence of the magnetization curves for α-MnO_2 nanorods under an external field of $H = 10$ kOe. Inset shows the variations of $d(\chi T)/dT$ with temperature, and (b) variations of the reciprocal of molar susceptibilities with temperature for high temperature data. Solid lines represent the fitting results in terms of the Curie–Weiss Law.

The observation of kink and hump in magnetization curves implies the existence of two transitions. The kink may correspond to a transition from antiferromagnetic to paramagnetic, while the magnetic transition for the hump should be associated with the trapped species of water and ammonia in the tunnel of α-MnO_2 nanorods, though its origin is not clear now. With regards to the magnetic transitions, Bragg et al., developed an analytic method to precisely derive the Néel temperature, T_N, by locating the peak position in $d(\chi T)/dT$ versus temperature [29]. We adopted this method to determine the Néel temperatures of our 1D α-MnO_2 nanostructures. As shown in inset of Fig. 8, $T_N = 25$ K is obtained for sample M220(5) as estimated from the $d(\chi T)/dt$–T plot. T_N values for sample M180(5) is 23.8 K. It is noted that the kink relating to this magnetic transition is difficult to see in sample M140(5). However, in the $d(\chi T)/dT$–T plot, there is a maximum at 22.8 K, which indicates a magnetic transition. It is also noted that all T_N's for all 1D α-MnO_2 are compatible with that of $T_N = 24.5$ K for needle-like α-MnO_2 [30], but are much higher than that of 13 K for α-MnO_2 nanowires [16].

Fig. 8(b) shows the variation of reciprocal of molar susceptibility with temperature. The high temperature

susceptibility data of 1D α-MnO followed well the Curie–Weiss law and therefore can be fitted to the following equation:

$$\chi = \chi_0 + \frac{C}{T-\theta}, \quad (5)$$

where θ is the Curie–Weiss temperature, C is the Curie–Weiss constant, and χ_0 represents the temperature-independent contribution which includes (1) the diamagnetic contributions due to ionic cores, (2) the Pauli paramagnetism due to conduction electrons, and (3) the Landau diamagnetic orbital contribution. The diamagnetic contribution from ionic core has the order of 10^{-7} emu/g as is calculated from the chemical formula. As is to be described elsewhere, our α-MnO_2 nanocrystals are semiconducting solids which is indicated by the conductivity of the order of $\sim 10^{-4}$ S/cm. For most of semiconducting materials, Paul paramagnetic contribution is about $\sim 10^{-7}$ emu/g [31]. Therefore, χ_0 term would approach zero. Consequently, $1/\chi$ and T should be linear. Data fitting in the temperature from 150 to 300 K yielded Weiss temperature (θ) and Curie constant (C), as listed in Table 1. The effective moments are 3.94, 3.97 and 4.04 μ_B for sample M140, M180 and M220 respectively, which are slightly larger than that expected for Mn^{4+} (3.87 μ_B), but far smaller than that for high spin Mn^{3+} (4.9 μ_B). This observation indicates that Mn ions are in a mixed valence state of Mn^{4+}/Mn^{3+}. Considering the very small magnetic moment of low spin Mn^{3+} (2.83 μ_B), Mn^{3+} ions in the present α-MnO_2 nanocrystals should be in high spin state. This is apparently different from potassium counterpart reported by Suib and co-workers [31], in which Mn^{3+} ions are considered to be in low spin states. Because the effective moment of Mn ions is the sum of the magnetic moment from each ion, Mn^{3+} and Mn^{4+}, the atomic fraction of Mn^{4+} out of the total Mn can be estimated to be 0.93, 0.90, and 0.83 for Mn140(5), Mn(180(5) and Mn220(5), respectively. Therefore, the average valence states of Mn ions are in the range of 3.93–3.83, which are very close to those determined by titration method. The Weiss temperatures θ of samples are in the range of −308 to −337 K. The largely negative θ value for our samples indicates a strong antiferromagnetic interaction between Mn moments.

4. Conclusions

This work reports on the preparation of highly crystalline 1D α-MnO_2 nanorods and their relevant structural and magnetic properties. By adjusting the ammonia concentration and reaction temperature, we achieved the single-phase α-MnO_2 nanorods with an orientation direction along c-axis. The formation of 1D α-MnO_2 proceeded via a transformation from γ- to α-MnO_2. The tunnel structure of 1D α-MnO_2 was modified by NH_4^+ and water molecules. The amount of NH_4^+ species trapped in the tunnels is almost independent on the reaction temperature, while that of water molecules entered in the tunnels increased with reaction temperature. The average diameter of α-MnO_2 nanorods increased from 9.2 to 16.5 nm when the reaction temperature increases from 140 to 220 °C. The finite size effects of these nanorods were characterized by the increase of antimagnetic transition temperature with rod diameter reduction. 1D α-MnO_2 nanostructures were kinetically unstable and would release NH_4^+ species and water molecule in the tunnels at high temperatures, which is accompanied by a structure transition from α-MnO_2 nanorods to cubic Mn_2O_3 nanorods. All 1D α-MnO_2 nanorods showed two magnetic transitions. The effective moments of Mn ions are in the range of 3.94–4.04 μ_B, slightly larger than Mn^{4+} (3.87 μ_B). Mn ions in 1D α-MnO_2 nanorods are in mixed valency of high spin state Mn^{4+}/Mn^{3+}.

Acknowledgments

This work was financially supported by NSFC under the contract (No. 20671092), National Basic Research Program of China (973 program, No. 2007CB613306), a grant from Hundreds Youth Talents Program of CAS (Li GS), in part by the fund of Fujian Key Lab of nanomaterials (2006L2005) and a Science and Technology Program from Fujian Province (No. 2005HZ01-1).

References

[1] (a) S.L. Brock, N.G. Duan, Z.R. Tian, O. Giraldo, H. Zhou, S.L. Suib, Chem. Mater. 10 (1998) 2619;
(b) R. Ghosh, Y.C. Son, V.D. Makwana, S.L. Suib, J. Catal. 224 (2004) 288;
(c) A. Goyal, M. Rajeswari, R. Shreekala, S.E. Lofland, S.M. Bhagat, T. Boettcher, C. Kwon, R. Ramesh, T. Venkatesan, Appl. Phys. Lett. 71 (1997) 2535.
[2] M.H. Huang, S. Mao, H. Feick, H.Q. Yan, Y.Y. Wu, H. Kind, E. Weber, R. Russo, P.D. Yang, Science 292 (2001) 1897.
[3] (a) X. Wang, Y.D. Li, Chem. Commun. 7 (2002) 764;
(b) X. Wang, Y.D. Li, Chem. Eur. J. 9 (2003) 300;
(c) X. Wang, Y.D. Li, J. Am. Chem. Soc. 124 (2002) 2880;
(d) F.Y. Cheng, J.Z. Zhao, W. Song, C.S. Li, H. Ma, J. Chen, P.W. Shen, Inorg. Chem. 45 (2006) 2038.
[4] Y. Muraoka, H. Chiba, T. Atou, M. Kikuchi, K. Hiraga, Y. Syono, S. Sugiyama, S. Yamamoto, J.C. Grenier, J. Solid State Chem. 144 (1999) 136.
[5] N. Kijima, T. Ikeda, K. Oikawa, F. Izumi, Y. Yoshimura, J. Solid State Chem. 177 (2004) 1258.
[6] Y. Tanaka, M. Tsuji, Mater. Res. Bull. 29 (1994) 1183.
[7] Z.Q. Li, Y. Ding, Y.J. Qing, Q. Yang, Y. Xie, Chem. Commun. 7 (2005) 918.
[8] R.N. Deguzman, Y.F. Shen, E.J. Neth, S.L. Suib, C.L. Oyoung, S. Levine, J.M. Newsam, Chem. Mater. 6 (1994) 815.
[9] S. Komaba, N. Kumagai, S. Chiba, Electrochim. Acta 46 (2000) 31.
[10] Q. Feng, T. Horiuchi, L.H. Liu, K. Yanagisawa, T. Mitsushio, Chem. Lett. 3 (2000) 284.
[11] F. Qi, H. Kanoh, K. Ooi, M. Tani, Y. Nakacho, J. Electrochem. Soc. 141 (1994) 135.
[12] F. Jean, C. Cachet, L.T. Yu, A. Lecerf, A. Quivy, J. Appl. Electrochem. 27 (1997) 635.
[13] Y. Tanaka, M. Tsuji, Y. Tamaura, Phys. Chem. Chem. Phys. 2 (2000) 1473.
[14] C.S. Johnson, M.M. Thackeray, J. Power Sources 97–98 (2001) 437.

[15] O. Giraldo, S.L. Brock, M. Marquez, S.L. Suib, H. Hillhouse, M. Tsapatsis, Nature 405 (2000) 38.
[16] J.B. Yang, X.D. Zhou, W.J. James, S.K. Malik, C.S. Wang, Appl. Phys. Lett. 85 (2004) 3160.
[17] Q. Li, F. Li, Q.D. Qiao, Liaoning Univ. Pet. Chem. Technol. 24 (2004) 11.
[18] D.C. Golden, C.C. Chen, J.B. Dixon, Science 231 (1986) 717.
[19] (a) Z.H. Liu, K. Ooi, Chem. Mater. 15 (2003) 3696;
(b) R. Ratheesh, G. Suresh, V.U. Nayar, J. Solid State Chem. 118 (1995) 341.
[20] G.Q. Zhang, S.J. Bao, X.G. Zhang, H.L. Li, J. Solid State Electrochem. 9 (2005) 655.
[21] P.M. De Wolff, Acta Crystallogr. 12 (1959) 341.
[22] Y. Chabre, J. Pannetier, Prog. Solid State Chem. 23 (1995) 1.
[23] P. Ruetschi, J. Electrochem. Soc. 131 (1984) 2737.
[24] T.X.T. Sayle, C.R.A. Catlow, R.R. Maphanga, P.E. Ngoepe, D.C. Sayle, J. Am. Chem. Soc. 127 (2005) 12828.
[25] G.S. Li, L.P. Li, J. Boerio-Goates, B.F. Woodfield, J. Am. Chem. Soc. 127 (2005) 8659.
[26] C.A. Barrero, J.D. Betancur, J.M. Greneche, G.F. Goya, T.S. Berquo, Geophys. J. Int. 164 (2006) 331.
[27] Z.H. Yang, Y.C. Zhang, W.X. Zhang, X. Wang, Y.T. Qian, X.G. Wen, S.H. Yang, J. Solid State Chem. 179 (2006) 679.
[28] J.H. Liang, Y.D. Li, Chem. Lett. 32 (2003) 1126.
[29] E.E. Bragg, M.S. Seehra, Phys. Rev. B 7 (1973) 4197.
[30] N. Yamamoto, T. Endo, M. Shimada, T Takada, Jpn. J. Appl. Phys. 13 (1974) 723.
[31] X.F. Shen, Y.S. Ding, J. Liu, Z.H. Han, J.I. Budnick, W.A. Hines, S.L. Suib, J. Am. Chem. Soc. 127 (2005) 6166.